OUKA
The University of Osaka
Institutional Knowledge Archive

Title	Influence of welding speed on mechanical properties and fracture behaviour of friction stir welded Haynes® 282 Ni superalloy
Author(s)	Sharma, Abhishek; Morisada, Yoshiaki; Ushioda, Kohsaku et al.
Citation	Materials Science and Engineering: A. 2025, 941, p. 148619
Version Type	VoR
URL	https://hdl.handle.net/11094/102611
rights	This article is licensed under a Creative Commons Attribution-NonCommercial-NoDerivatives 4.0 International License.
Note	

The University of Osaka Institutional Knowledge Archive : OUKA

https://ir.library.osaka-u.ac.jp/

The University of Osaka

Materials Science & Engineering A 941 (2025) 148619

Contents lists available at ScienceDirect

Materials Science & Engineering A

journal homepage: www.elsevier.com/locate/msea

Influence of welding speed on mechanical properties and fracture behaviour of friction stir welded Haynes® 282 Ni superalloy

Abhishek Sharma [a,*], Yoshiaki Morisada [a], Kohsaku Ushioda [a], Sukhdeep Singh [b], Hidetoshi Fujii [a,**]

[a] Joining & Welding Research Institute, The University of Osaka, Osaka, 567-0047, Japan
[b] Department of Engineering Science, University West, Trollhättan, SE-46186, Sweden

ARTICLE INFO

Keywords:
Friction stir welding (FSW)
Haynes 282
Ni superalloy
Fracture
Precipitation strengthening

ABSTRACT

This study investigates the joining of gamma prime (γ′)-strengthened Haynes® 282 (H282) Ni superalloy using Friction Stir Welding (FSW) with a novel hemispherical dome-shaped tool at different welding speeds. After post-welding heat treatment (PWHT), the stir zone (SZ) of the joints, regardless of welding speed, exhibited a tensile strength of approximately 1360 MPa, compared to the base metal strength (subjected to the same PWHT) of about 1144 MPa, resulting in a UTS-based joint efficiency of 100 %. The microstructural analysis identified primary Ti- and Mo-rich (MC) carbides, secondary Cr-rich ($M_{23}C_6$) carbides, and γ′ precipitates as key constituents within the austenitic γ matrix after PWHT. During FSW, the plastic deformation and material flow significantly altered the dispersion characteristics of brittle intergranular MC carbides, transforming them from an intergranular interconnected network (colonies) in the BM to discrete carbides that are randomly dispersed at the grain boundaries in the SZ. The increased strength of the SZ is attributed to this dispersion transformation, as the primary MC carbides are the preferential sites for the void nucleation during tensile loading. Increased welding speed led to reduced frictional heat input, resulting in finer grain size and increased local elongation while maintaining similar weld strength. Therefore, the microstructure of the H282 alloy is minimally impacted by the frictional heat input across various process parameters during FSW. This finding underscores the advantages of FSW for H282 alloy over other fusion welding techniques, where precise control of process parameters is crucial to prevent elemental segregation in the fusion zone.

1. Introduction

Haynes® 282 (H282) is a gamma prime (γ′) precipitation-strengthened Ni-based superalloy that is used for high-temperature structural applications in jet engines and advanced ultra-supercritical thermal power plants [1]. The unique combination of excellent creep properties (in the temperature range 650–920 °C), thermal stability, and formability makes H282 a superior candidate material for high-temperature applications as compared to the commonly used superalloys such as Inconel 718, Waspaloy, Rene 41, etc. [2].

Welding is a crucial aspect of fabrication in turbine engine assembly, used to join both simple and complex components. Additionally, welding is also extensively used for the repair and remanufacturing of service-damaged components, particularly in applications such as turbine engines, where harsh and hostile environments make the component more susceptible to cracking [3]. The annealed H282 alloy demonstrates good weldability for a γ′ strengthened alloy, including satisfactory resistance to strain-age cracking [4]. However, fusion welding (such as Laser beam Welding (LBW)) of H282 alloy frequently results in microsegregation and non-equilibrium phase transformation in the weldments during solidification [5]. The dendritic microsegregation leads to the formation of intermetallic secondary solidification phases along the dendrite interstices and inhomogeneous dispersion of secondary phase precipitates [6]. Sometimes, the strengthening carbides (MC, M_6C, $M_{23}C_6$, etc.) also segregate in the interdendritic regions and deteriorate the material's performance at elevated temperatures [7,8]. The grain boundary liquation and cracking in the heat-affected zone (HAZ) of H282 alloy was also reported by various researchers [9–11].

Friction stir welding (FSW) is a solid-state joining technique that

* Corresponding author.
** Corresponding author.
E-mail addresses: sharma.abhishek.jwri@osaka-u.ac.jp (A. Sharma), fujii.hidetoshi.jwri@osaka-u.ac.jp (H. Fujii).

https://doi.org/10.1016/j.msea.2025.148619
Received 19 January 2025; Received in revised form 22 May 2025; Accepted 1 June 2025
Available online 3 June 2025
0921-5093/© 2025 The Authors. Published by Elsevier B.V. This is an open access article under the CC BY-NC-ND license (http://creativecommons.org/licenses/by-nc-nd/4.0/).

Table 1
EDS analysis of the carbides shown in Fig. 4(a) and (b).

Analysis point	Al	Ti	Cr	Mo	Ni	Others
1 - MC	–	59.03	2.47	35.52	–	2.98
2 – $M_{23}C_6$	2.21	4.03	29.54	9.99	54.23	–

offers a potential solution to the abovementioned problems, usually associated with the fusion welding of H282 alloy. However, the limitations of FSW, including significant tool wear, probe fracture, and high forces, have hindered extensive research on H282 alloy. As a result, only two studies are available on this alloy's FSW to date. The first, conducted by Komarasamy et al. [12], demonstrated a successful FSW of H282 alloy, achieving 100 % joint efficiency. The authors employed a Polycrystalline Cubic Boron Nitride (PCBN) tool, combined with argon shielding and water cooling, to manage tool fracture, oxidation, and high temperatures during the FSW process. Mukuda et al. [13] introduced an innovative hemispherical dome-shaped tool tilted toward the retreating side (RS). This design offers several benefits, including reduced frictional heat generation due to the absence of a shoulder and enhanced resistance to breakage, as it eliminates the cylindrical probe that is susceptible to fracture during FSW of high-strength, high--temperature metallic materials. Subsequently, Ambrosio et al. [14,15] reported the application of the hemispherical dome-shaped tool for FSW of aluminum alloys and the dissimilar lap joining of AA6061 with mild steel. The second study on the joining of H282 alloy by using FSW was recently reported by Sharma et al. [16] where the authors used this hemispherical dome-shaped tool made of silicon nitride (Si_3N_4) to successfully join the alloy. This tool profile effectively minimized heat generation, resulting in 100 % joint efficiency and negligible tool wear at a low welding speed of 30 mm/min and a tool rotational speed of 400 RPM. The promising results of this study, particularly regarding joint efficiency and microstructural evolution, motivate the present research. The present investigation addresses a key question related to the joining of H282 alloy by using a hemispherical tool, i.e., the impact of a critical process parameter, welding speed, on joint strength and microstructural development. Furthermore, a detailed fracture analysis is conducted to investigate the void nucleation and dominant fracture mechanism in the stir zone (SZ) of the FSWed H282 alloy.

2. Materials & methods

Soft annealed wrought H282 plates of dimensions 100 mm (l) x 50 mm (w) x 3.2 mm (t) were used as a base material. Table 1s (supplementary information) lists the elemental chemical composition of the base material.

FSW was performed on H282 alloy plates using a "bead-on-plate" configuration in a position control setup, with an integrated load cell for monitoring axial force. The process parameters included a constant tool rotational speed of 400 RPM, a 7° tilt angle towards the RS, and a 2.5 mm plunge depth. Joints were fabricated at 30, 100, and 200 mm/min welding speeds. The welding temperatures were measured using thermal imaging with an emissivity of 0.9. A hemispherical tool made of Si_3N_4, with a dome diameter of 15 mm, was used for the FSW process. Fig. 1 provides a schematic representation of the overall FSW setup and tool geometry. In Fig. 1, the schematic representation of the cross-section demonstrates an interaction between the hemispherical dome and the base plate. The amount of material plastically deformed by the hemispherical tool during FSW is indicated by the term "interaction volume".

After welding, the joint specimens were subjected to a two-step post-weld heat treatment (PWHT) according to the recommendations of Haynes International. The steps included: (i) aging at 1010 °C for 2 h, followed by air cooling (AC), and (ii) aging at 788 °C for 8 h, followed by AC. Notably, all the results presented here correspond to the PWHT specimen and BM specimen aged at the same time-temperature conditions as the PWHT.

The specimens for tensile testing (transverse) and microstructural observation were obtained using electrical discharge machining (EDM). The weld bead and keyhole profile were measured by using an optical surface profilometer (Keyence, VR3200). Microstructural characterization was conducted on a field emission scanning electron microscope (SEM, JEOL JSM-7001FA) equipped with an electron back-scattered diffraction (EBSD) and energy dispersive spectroscopy (EDS) attachments. Metallographic sample preparation for SEM and EBSD analysis involves paper polishing (progressively up to 4000 grit size) and diamond polishing (1 μm), followed by electropolishing. The electropolishing was conducted in a solution of perchloric acid, ethanol, and 2-butoxyethanol at 16V for 8 s. The thin foil specimens for the

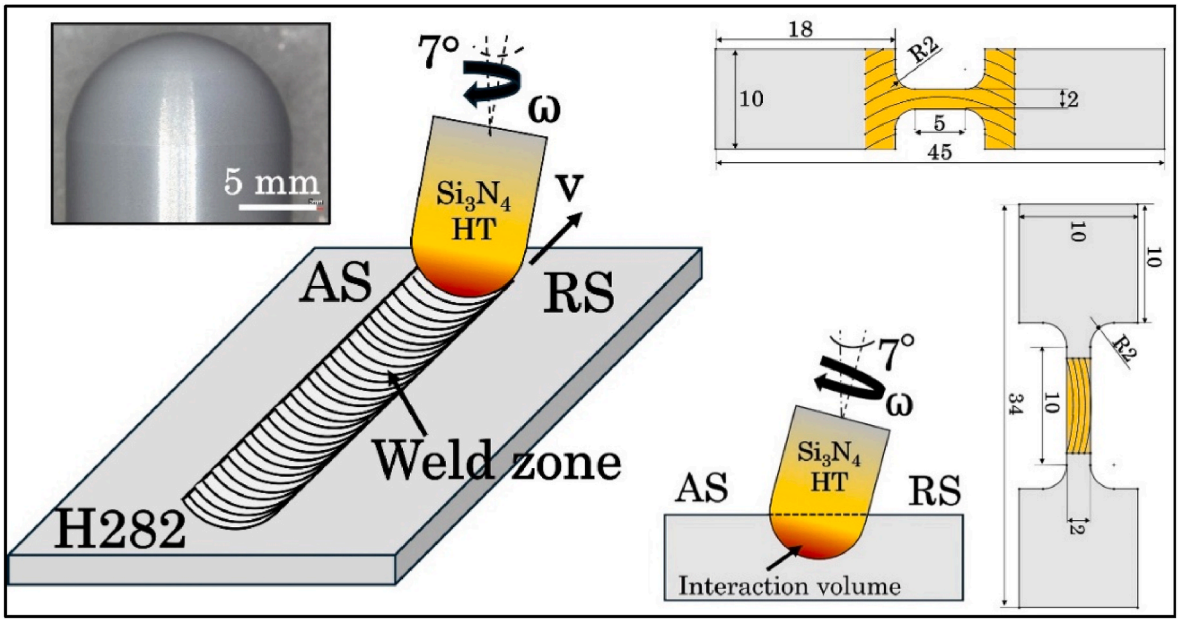

Fig. 1. Schematic representation of FSW with the hemispherical tool tilted towards RS and tensile test scheme. (The inset shows the picture of the hemispherical tool).

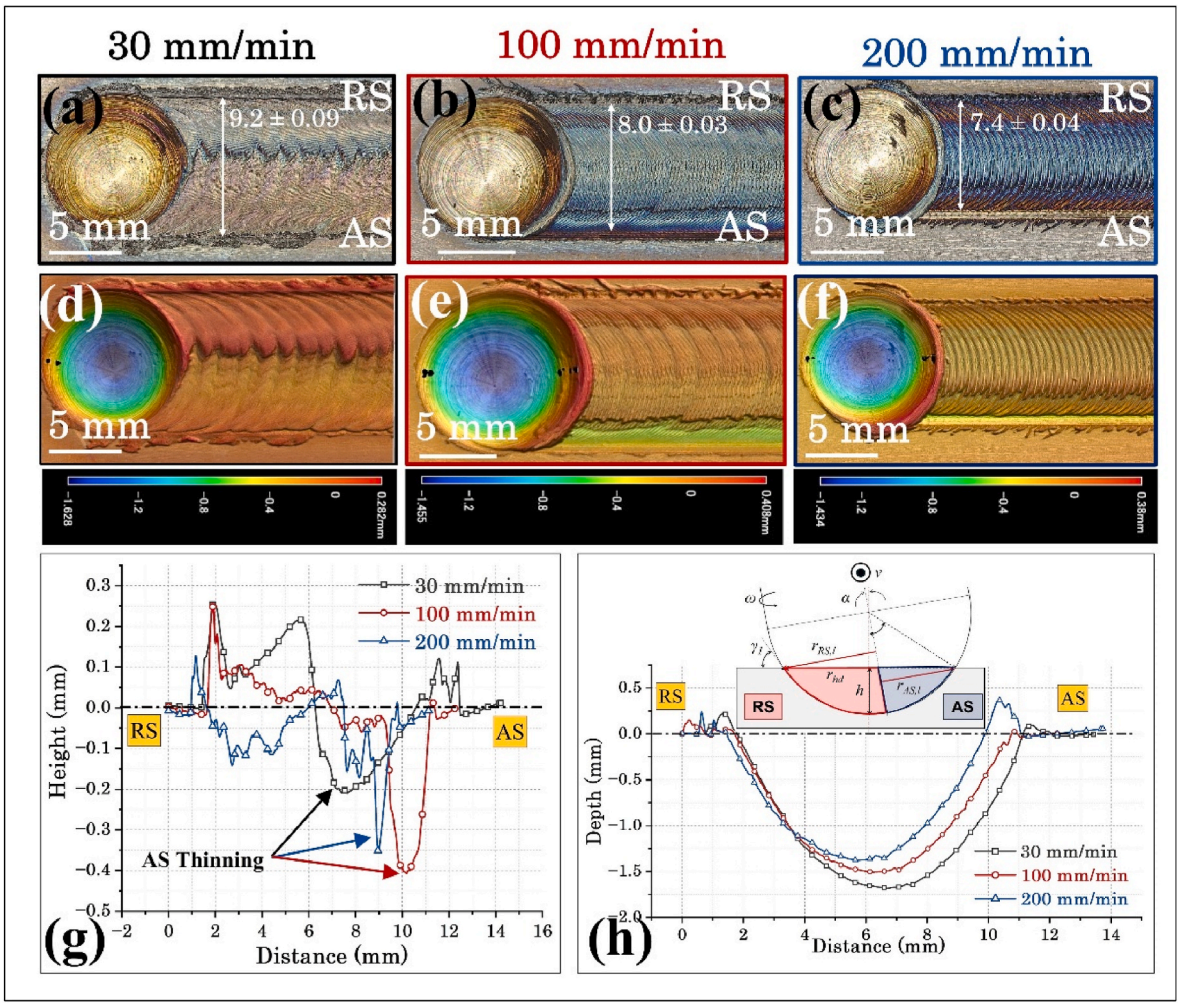

Fig. 2. (a–c) Weld quality obtained at a welding speed of 30, 100, and 200 mm/min, respectively, (d–f) surface profile of the welds, (g) weld thickness profile, and (h) keyhole profile representing the effective plunge depth (EPD).

transmission electron microscope (TEM, JEOL 2100F) characterization of the welded specimens were obtained using a focused ion beam milling (FIB, Hitachi FB-2000S). The TEM specimens were obtained from the longitudinal cross-section of the fractured tensile specimens.

The microhardness measurement was obtained by using a Vickers microhardness tester (Future Tech, FM-800) at a load of 100 kgf and a dwell time of 15 s. The microhardness measurements were conducted at 0.5 mm and 1 mm distances along the thickness of the welded specimen. More than 60 indents were recorded at each location with an inter-indent distance of ~250 μm. The uniaxial tensile testing was conducted on two types of tensile specimens, i.e., standard and miniaturized specimens. In the standard specimen, the weld zone was located at the center of the gauge length. Meanwhile, in the miniaturized specimen, the gauge length encompasses only the SZ. The standard and miniaturized tensile test specimens were paper ground up to 0.5 mm on the FSW surface, followed by grinding the rear surface to a final specimen thickness of 1.6 ± 0.05 mm. The tensile testing was conducted on the universal testing machine (Instron, 5500R) with a loading rate of 0.6 mm/min. The tensile strain was measured by using a digital image correlation (DIC) as per the method reported elsewhere [17].

3. Results

3.1. Weld quality, temperature, and force measurement

Fig. 2(a–c) illustrates the weld surface produced at welding speeds of 30, 100, and 200 mm/min, respectively. Fig. 2(d–f) represents the surface profile of the welds as measured from the optical surface profilometer. Fig. 2 (g) and (h) present quantitative analyses of the weld bead profile and the keyhole profile, respectively. As the welding speed increases from 30 to 200 mm/min, the weld zone's width decreases, as evident in Fig. 2(a–c). At higher welding speeds, the reduction in frictional heat generation also results in diminished plastic deformation of the material, leading to a smaller volume of material flowing through the weld zone. Consequently, the interaction volume also reduces with the increasing welding speed as discussed later in this paper. Therefore, the effective plunge depth (EPD), shown in Fig. 2 (g), and the cross-sectional width of the joint both decrease with increasing welding speed.

Fig. 2 (g) demonstrates that on the advancing side (AS), joint thickness is reduced (or AS thinning) under all three welding conditions. The AS thinning is primarily attributed to the complex material flow associated with the hemispherical dome profile of the tool and the tilt angle towards the RS. The material flow mechanism leading to this characteristic AS thinning feature is reported elsewhere by Ambrosio et al. [18]. At 30 mm/min, AS thinning is minimal, with the width covering approximately half of the weld bead. At 100 mm/min, the weld bead thickness becomes more uniform across the weld width, exhibiting a narrow, groove-like AS thinning. When the welding speed is increased to 200 mm/min, non-uniform material flow occurs, leading to thinning on both the AS and the RS, with a plateau in the center. This effect is attributed to significantly reduced heat generation, which is insufficient for adequate plastic deformation of the material. In successful FSW

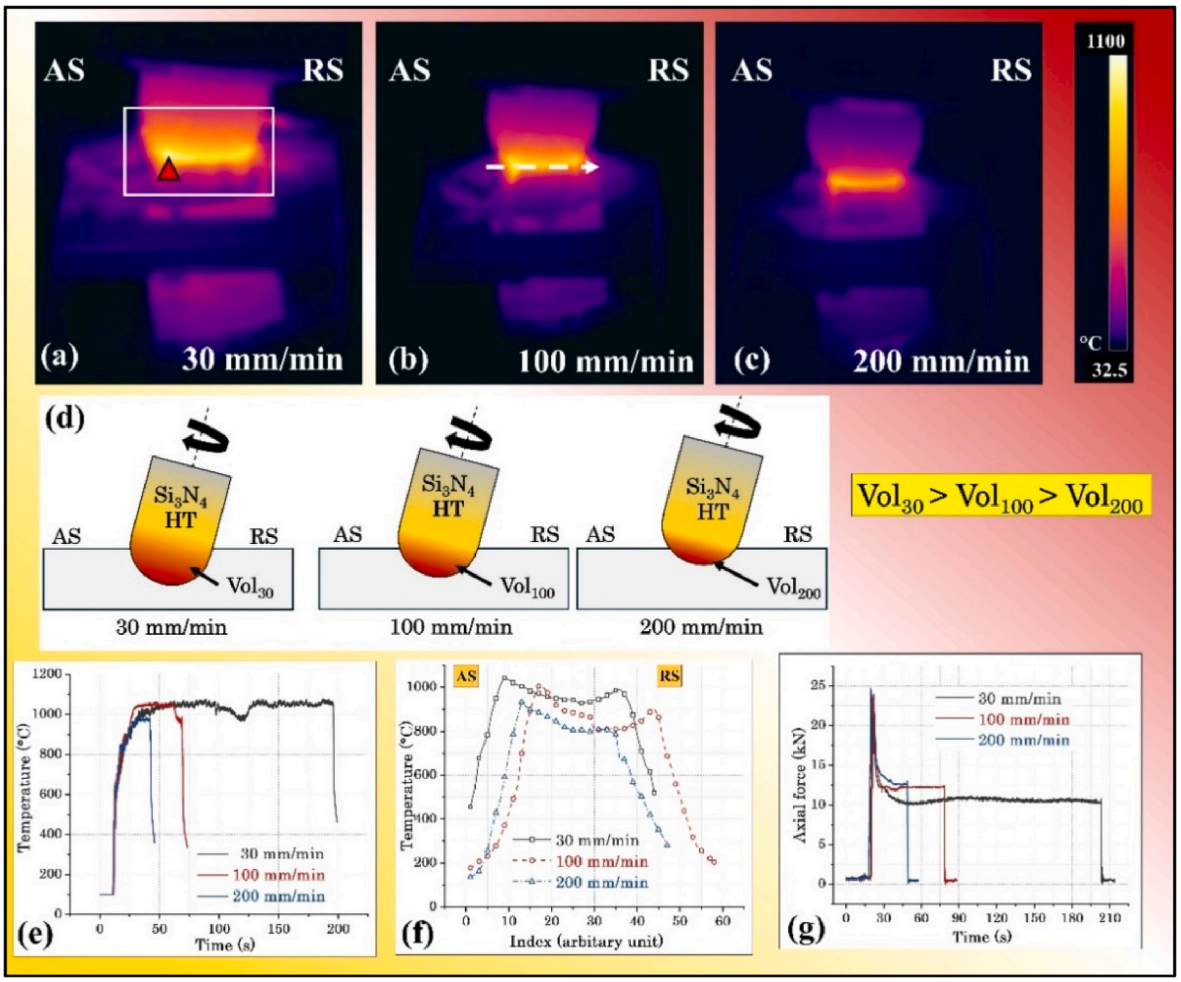

Fig. 3. Thermal images of the welds fabricated at 30, 100, and 200 mm/min, respectively, (d) schematic representation of interaction volume at different welding speeds, (e) maximum temperature profile measured at AS, (f) temperature gradient profile at AS and RS, (g) axial force measurement.

joints, the material on the AS flows toward the RS at the leading edge, and at the trailing edge, the material flows from the RS to the AS [19]. However, at a welding speed of 200 mm/min, insufficient plastic flow causes material on the AS (on the leading side) to deposit at the center of the weld zone instead of reaching the RS side. Similarly, at the trailing edge, material generated at the RS settles at the center instead of flowing to the AS. This results in thinning on the AS and RS, with a plateau in the center.

Fig. 3 illustrates various thermal and mechanical aspects of FSWs with the hemispherical tool at different welding speeds. Thermal images obtained at welding speeds of 30, 100, and 200 mm/min are shown in Fig. 3(a–c), respectively. Fig. 3 (d) schematically represents the variation in interaction volume with welding speed, which decreases as the welding speed increases. This reduction in interaction volume is also evident in the thermal images (Fig. 3(a–c)). Regardless of welding speed, the maximum temperature consistently occurs on the AS of the weld. Fig. 3 (e) depicts the maximum temperature profile measured on the AS, corresponding to the thermal image in Fig. 3 (a). Similarly, Fig. 3 (f) presents the temperature gradient between the AS and RS, measured along the line shown in Fig. 3 (b). Fig. 3 (g) displays the axial force recorded at different welding speeds. From Fig. 3 (e), it can be observed that the average maximum temperature on the AS is approximately 1035 °C at welding speeds of 30 and 100 mm/min, remaining relatively constant during the welding process. However, at a 200 mm/min welding speed, the average maximum temperature significantly decreases to approximately 980 °C. Fig. 3 (f) highlights an increasing peak temperature gradient between the AS and RS as welding speed rises, with the peak temperature consistently located on the AS. This increase in the temperature gradient is attributed to asymmetric material flow and heat generation due to the reduced interaction volume at higher welding speeds during FSW. Finally, Fig. 3 (g) shows that frictional heating at the tool/substrate interface decreases as welding speed increases, resulting in a rise in axial force during welding.

3.2. Microstructural evolution and constituent phases

Fig. 4(a) and (b) show the backscattered SEM (BS-SEM) micrographs of the two-step aged as-received wrought H282 alloy (referred to as base metal, BM throughout). The presence of coherent γ′ precipitates in the grain interior can be confirmed. Additionally, the interconnected primary Ti- and Mo-rich MC carbides and secondary Cr-rich $M_{23}C_6$ carbides precipitated along the grain boundaries can be visualized in the aged microstructure. The EDS analysis-based chemical composition of the carbide phases is illustrated in Table 1. Our previous study also confirmed the presence of γ′ precipitates, MC and $M_{23}C_6$ carbides through selected area electron diffraction (SAED) pattern in the as-received and PWHT FSWed H282 alloy [16]. Fig. 4 (c) shows the EBSD-inverse pole figure (IPF) map of the BM specimen with the corresponding grain size distribution shown in Fig. 4 (d). The microstructure consists of a coarse-grained structure with an average grain size of ~54 μm. The presence of deformation twins can also be visualized from the EBSD-IPF map.

Fig. 5 (a–b), (c-d), and (e-f) show the SEM micrographs from the SZ of the welds fabricated at a welding speed of 30, 100, and 200 mm/min,

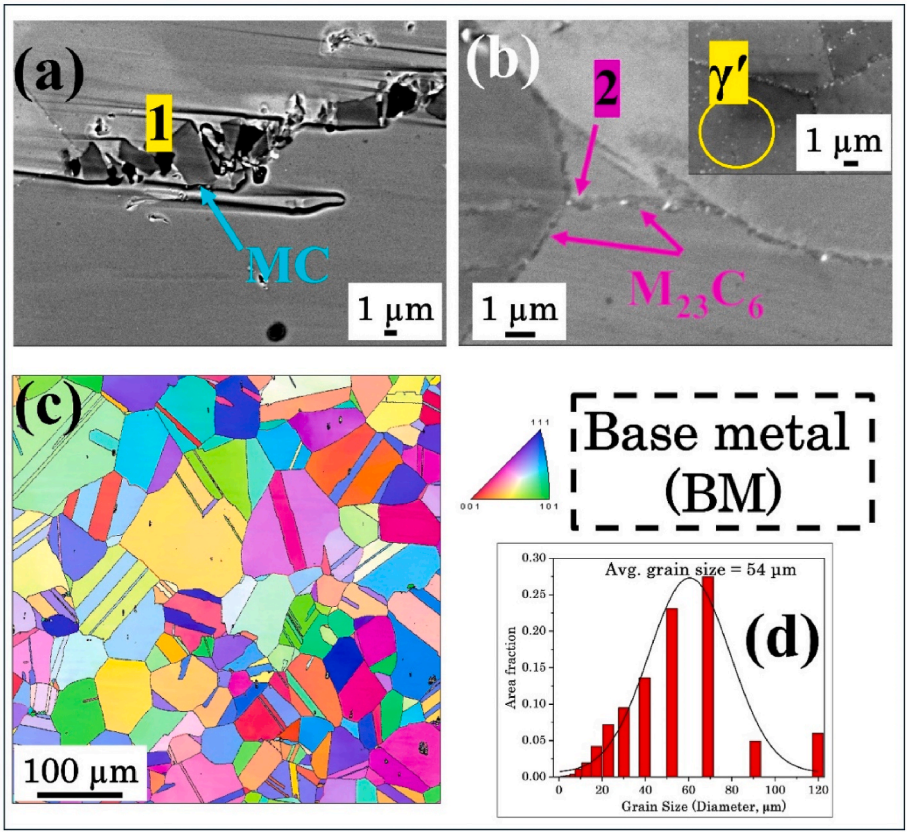

Fig. 4. (a–b) BS-SEM micrographs, (c) EBSD-IPF map, and (d) grain size distribution of aged BM.

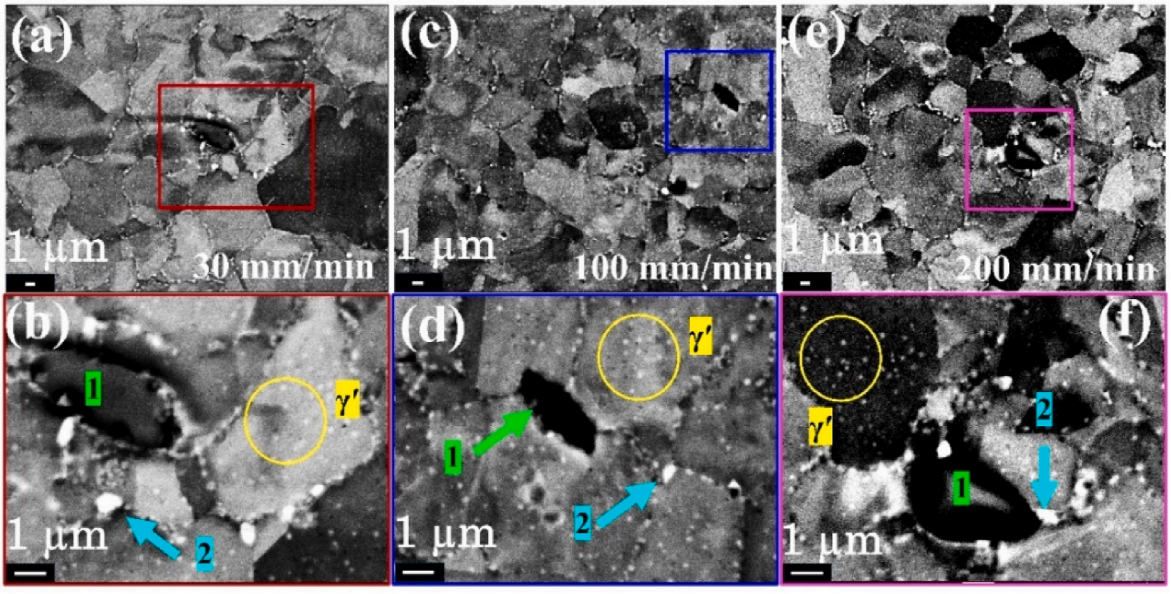

Fig. 5. SEM micrographs of PWHT FSWs fabricated at (a–b) 30, (c–d) 100, and (e–f) 200 mm/min, respectively.

respectively. The fine-grained microstructure (compared to BM), along with the γ' phase, MC, and $M_{23}C_6$ carbides, can be observed here. The MC (Ti- and Mo-rich) and $M_{23}C_6$ (Cr-rich) carbides in Fig. 5(b, d, and f) are identified based on the EDS analysis documented in Table 2. The grain refinement during FSW resulted in an increased grain boundary (GB) area within the SZ of the joint as compared to the BM. As a result, the nucleation sites for the precipitation of secondary $M_{23}C_6$ carbides during the PWHT also increased, leading to a higher volume fraction of secondary carbides in the FSWed joints as compared to BM and discussed later in this paper.

Fig. 6 represents an interesting finding regarding the distribution pattern of the primary MC carbides in the FSWed region compared to the BM. In BM (Fig. 6 (a)), the MC carbides are segregated at the high-angle grain boundaries in the form of interconnected particles (or colonies).

Table 2
EDS analysis of the particles shown in Fig. 5(b), (d), and (f).

Analysis point	Al	Ti	Cr	Mo	Ni	Others
FSW – 30 mm/min						
1 - MC	–	56.13	3.32	34.39	3.42	2.74
2 – $M_{23}C_6$	1.30	2.70	29.40	16.46	49.02	1.12
FSW – 30 mm/min						
1 - MC	–	53.63	4.45	31.89	7.62	2.42
2 – $M_{23}C_6$	1.46	2.60	23.35	11.09	61.51	–
FSW – 30 mm/min						
1 - MC	–	56.60	2.24	36.26	2.87	2.04
2 – $M_{23}C_6$	1.60	3.63	32.66	18.16	43.94	–

These colonies consist of both fine and coarse agglomerated MC carbides. However, the interparticle distance of these MC carbide particles is very short and cannot be measured by the traditional methods. The average size of these colonies (b_{avg}) is ~10 μm, as shown in Fig. 7 (a). Whereas, in the FSWed region (at all welding speeds), the MC carbides are preferentially dispersed at the grain boundaries as discrete particles, as shown in Fig. 6(b–d). The average size of these singly dispersed MC carbides is ~3 μm (see Fig. 7(b–d)). Interestingly, from Fig. 6, it can also be observed that the individual particle size of MC carbides in the BM and FSWed region is almost similar. However, the distribution pattern inside the matrix is uniform in the FSWed region compared to the colonies-like dispersion in the BM.

Fig. 8 (a) and (b) show the low magnification through-thickness EBSD grain size maps of the joints fabricated at a welding speed of 30 and 200 mm/min, respectively. Fig. 8 (c–d), (e-f), and (g-h) represent the EBSD-IPF maps of the welds fabricated at 30, 100, and 200 mm/min, respectively. The EBSD IPF measurement was observed at two locations inside the SZ, namely, at the top and the bottom regions as shown by the white square sections marked in Fig. 8 (a) and (b).

The low magnification grain size map in Fig. 8 (a), corresponding to a welding speed of 30 mm/min, illustrates the grain size gradient across the thickness of the weld zone. The upper region, near the tool/substrate interface, exhibits a fine grain structure, which progressively coarsens towards the lower part of the weld zone. In contrast, at a welding speed of 200 mm/min (Fig. 8 (b)), the grain size remains consistently fine throughout the weld zone, with only a small fraction of coarse grains appearing at the top. At 30 mm/min welding speed, the larger frictional contact area between the tool and substrate results in a greater volume of material flow across the weld thickness. This, combined with the lower welding speed, increases heat generation, leading to grain coarsening at the bottom of the SZ. In comparison, the reduced frictional contact area (or interaction volume) and higher welding speed at 200 mm/min reduce heat dissipation across the thickness, maintaining a fine grain structure throughout the lower part of the weld zone. This observation is further confirmed by the EBSD-IPF maps and average grain size values. The average grain size at the top of the weld zone remains almost similar across all welding speeds (Fig. 8(c, e, g)), while at the bottom of the SZ, the grain size decreases as welding speed increases.

3.3. Mechanical properties

Fig. 9 (a) shows the nominal tensile stress-strain curves of the aged BM and PWHT FSWed specimen obtained at different welding speeds of 30, 100, and 200 mm/min. The corresponding mechanical properties are listed in Table 3. The tensile specimens corresponding to Fig. 9 (a) were the standard tensile specimens with the weld zone located only at the center of the gauge length. In these specimens, the fracture occurred on the RS in the base metal region. Therefore, these specimens are abbreviated as base metal zone (BMZ) fractured specimens. Interestingly, the fracture in the base metal region indicates a higher tensile strength of the FSWed joints as compared to the base metal, indicating a joint efficiency of ~100 %. Since the specimens were fractured in the base metal region, the ultimate tensile strength (UTS) of these specimens is exactly equal to the base metal (see Fig. 9 (a)). However, the BMZ-fractured specimens exhibit a noticeable increase in yield strength (YS) compared to the aged base metal, as shown in Table 3. Since fracture occurred in the base metal region, the YS is ideally expected to be similar to that of the aged base metal. To investigate this discrepancy, hardness mapping (see Fig. 1(s), supplementary information) was performed on the 30 mm/min specimens in both the as-welded and PWHT conditions. The results reveal a higher-hardness intermediate zone (IZ) between the heat-affected zone (HAZ) and the base metal in the as-welded specimen. This increased hardness is likely due to the precipitation of fine γ' particles caused by the thermal cycle during FSW. During PWHT, the IZ appears to retain a higher volume fraction of γ' phase compared to the base metal, contributing to the enhanced YS observed in the BMZ-fractured specimens. However, further evidence is needed to fully validate this hypothesis. Additionally, the elongation is reduced drastically from ~31 % in the BM specimen to ~12–16 % in the BMZ fractured specimens. The reduced elongation can be ascribed to the deformation resistance offered by the strengthened weld region upon uniaxial tensile loading and fine γ' precipitates in the IZ. While microstructural characterization was conducted in the SZ of the welds, the

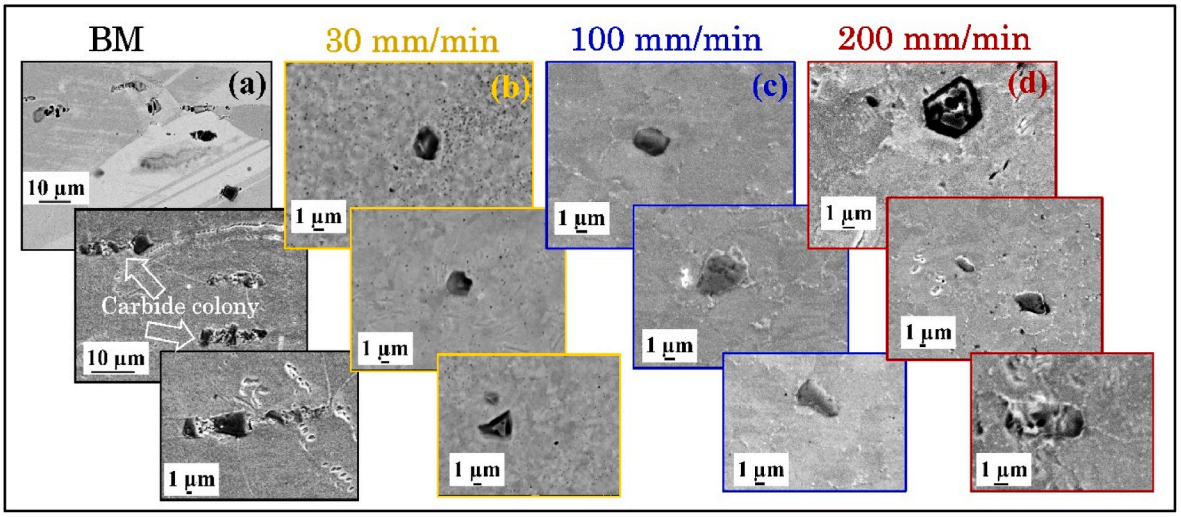

Fig. 6. MC carbide distribution in (a)aged BM, and PWHT FSWed specimens at (b) 30, (c) 100, and (d) 200 mm/min.

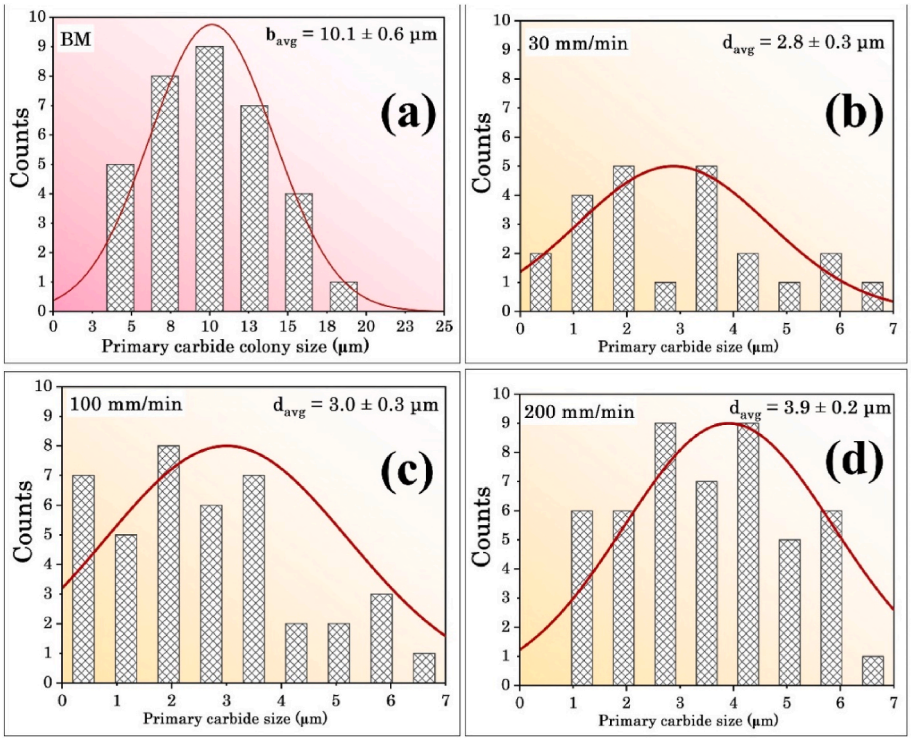

Fig. 7. Quantitative distribution of MC carbide colonies in (a) aged BM, and MC carbide particles in PWHT FSWed specimens at (b) 30, (c) 100, and (d) 200 mm/min (the red curve indicates the normal distribution). (For interpretation of the references to colour in this figure legend, the reader is referred to the Web version of this article.)

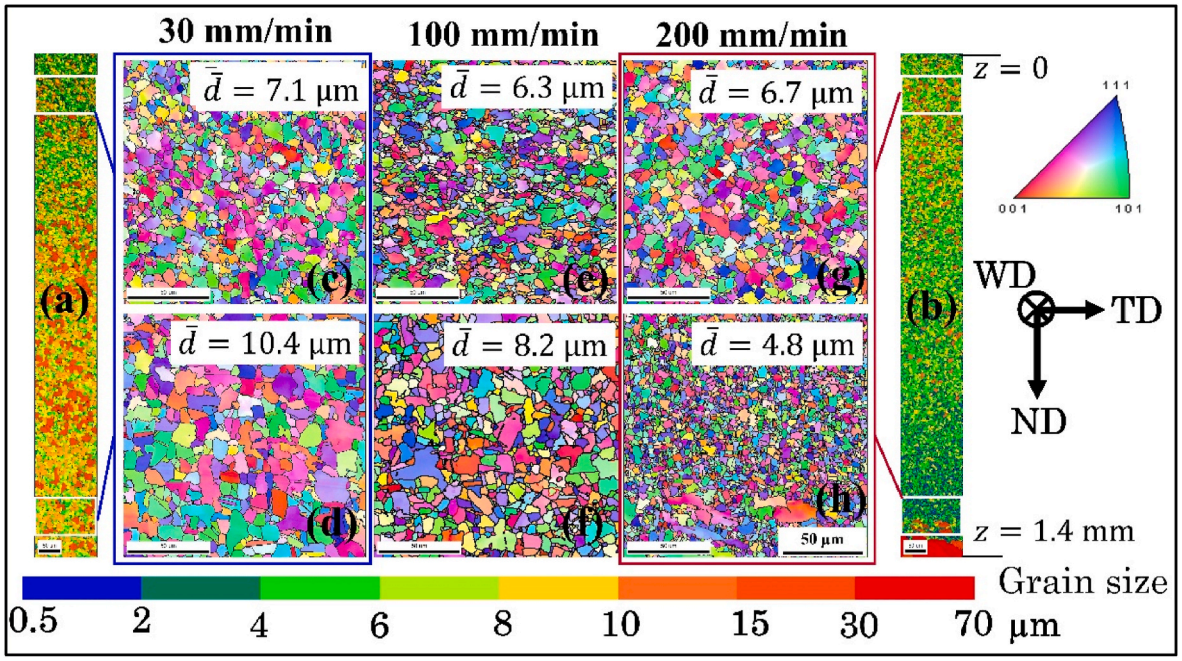

Fig. 8. Through thickness EBSD grain size maps of PWHT welds fabricated at (a) 30, (b) 200 mm/min. EBSD IPF maps of welds corresponding to the welding speed of (c–d) 30, (e–f) 100, and (g–h) 200, mm/min. White rectangles in Fig. (a) and (b) indicate the scan locations for the IPF maps. (z indicates the distance from the top surface). (The colours in (a) and (b) represents the grain size according to the colour coded scale shown at the bottom. Whereas the colours in (c–h) represents the crystal orientation as per the IPF shown at the right). (For interpretation of the references to colour in this figure legend, the reader is referred to the Web version of this article.)

fracture occurring in the base metal region prevented a direct correlation between the microstructure and mechanical properties.

Therefore, the miniaturized tensile specimens with the SZ as the gauge length were used to predict the exact mechanical properties of the welded joints. These specimens are referred to as SZ fractured specimens, hereafter. Fig. 9 (b) shows the nominal tensile stress-strain curves obtained from the SZ fractured specimens. The UTS and YS of the specimens welded at different welding speeds were almost the same

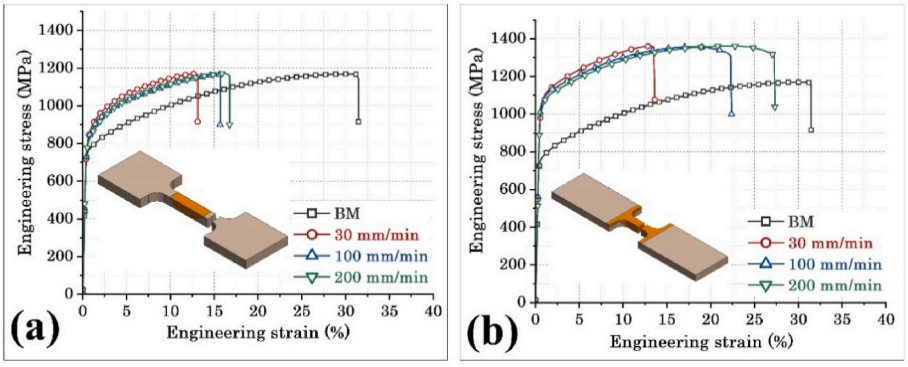

Fig. 9. Nominal tensile stress-strain curves of PWHT (a) BMZ, and (b) SZ fractured specimens.

Table 3
Mechanical properties obtained from stress-strain curves.

Specimen	UTS (MPa)	YS (MPa)	TE (%)	UE (%)	LE (%)
aged BM specimen	1144 ± 6	738 ± 7	36 ± 0.2	32 ± 0.1	4.2 ± 0.2
PWHT BMZ fracture specimen					
30 mm/min	1173 ± 6	836 ± 10	13.8 ± 1.2	13.3 ± 1.4	0.5 ± 0.1
100 mm/min	1169 ± 20	815 ± 11	17.0 ± 1.1	16.2 ± 0.8	0.8 ± 0.3
200 mm/min	1173 ± 4	793 ± 13	17.2 ± 0.3	16.2 ± 0.6	1.0 ± 0.2
PWHT SZ fracture specimen					
30 mm/min	1370 ± 24	1059 ± 9	15.0 ± 1.5	14.4 ± 1.3	0.6 **± 0.1**
100 mm/min	1358 ± 15	1057 ± 11	23.8 ± 1.1	18.4 ± 0.7	5.4 ± 0.4
200 mm/min	1361 ± 4	1050 ± 5	28.0 ± 2.1	22.0 ± 1.08	6.0 ± 0.9

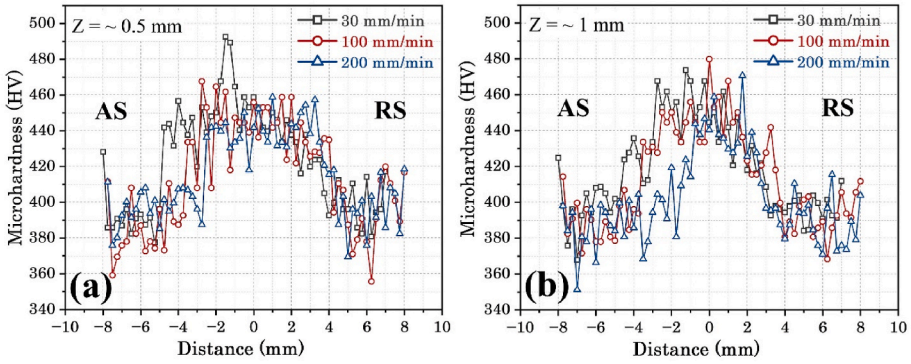

Fig. 10. Microhardness distribution of PWHT welds at a thickness of (a) 0.5 mm, and (b) 1 mm from the weld top.

ranging to ~ 1360 MPa and 1050 MPa, respectively. Interestingly, the SZ strength was ~20 % higher than the BM specimen giving a joint efficiency of ~100 %. Although, the welding speed has a negligible effect on the UTS and YS of the joint, the total (TE), uniform (UE), and local (LE) elongation increases with the increasing welding speed. The increase in LE from approximately 0.6 % in the joint fabricated at 30 mm/min to around 5.4 % and 6 % in the joints FSWed at 100 and 200 mm/min, respectively, can be attributed to the finer grain structure achieved at higher welding speeds, as shown in Fig. 8(a) and (b). Takebe and Ushioda [20] reported a general relationship between grain size and local elongation, where voids tend to form near the grain boundaries. In finer grains, the growth of these voids is limited since stress does not concentrate easily, leading to an expansion of the necking region and consequently higher local elongation.

Fig. 10(a) and (b) show the microhardness variation of the FSWed specimens measured at a depth of 0.5 and 1 mm from the tool/substrate interface, respectively. Firstly, at both 0.5- and 1-mm thickness, the SZ of the FSWed joints displayed a higher microhardness as compared to the average microhardness of the BM (~416 ± 21 HV). Secondly, at 200 mm/min, the hardness distribution indicates that the width of the weld zone reduces sharply and becomes narrower with the increased distance (Z = 1 mm, Fig. 10 (b)) from the tool/substrate interface. This reduced width of the weld zone is attributed to the reduced interaction volume and EPD as discussed in Fig. 3. Fig. 10(a) and (b) also indicates an overall uniform and higher hardness obtained at the welding speed of 30 and 100 mm/min.

3.4. Fractography

Fig. 11(a–c) and (d-f) show low magnification fractography of the BMZ and SZ fractured specimens, respectively. The BMZ fractured specimens (across all welding speeds) exhibit a coarse-grained, intergranular ductile fracture, with ductile GB tearing observable at various locations. In contrast, the SZ fractured specimens (Fig. 11(d–f)) display a fine-grained, intergranular ductile fracture. However, the specimens welded at 100 and 200 mm/min welding speeds reveal a coarse-grained,

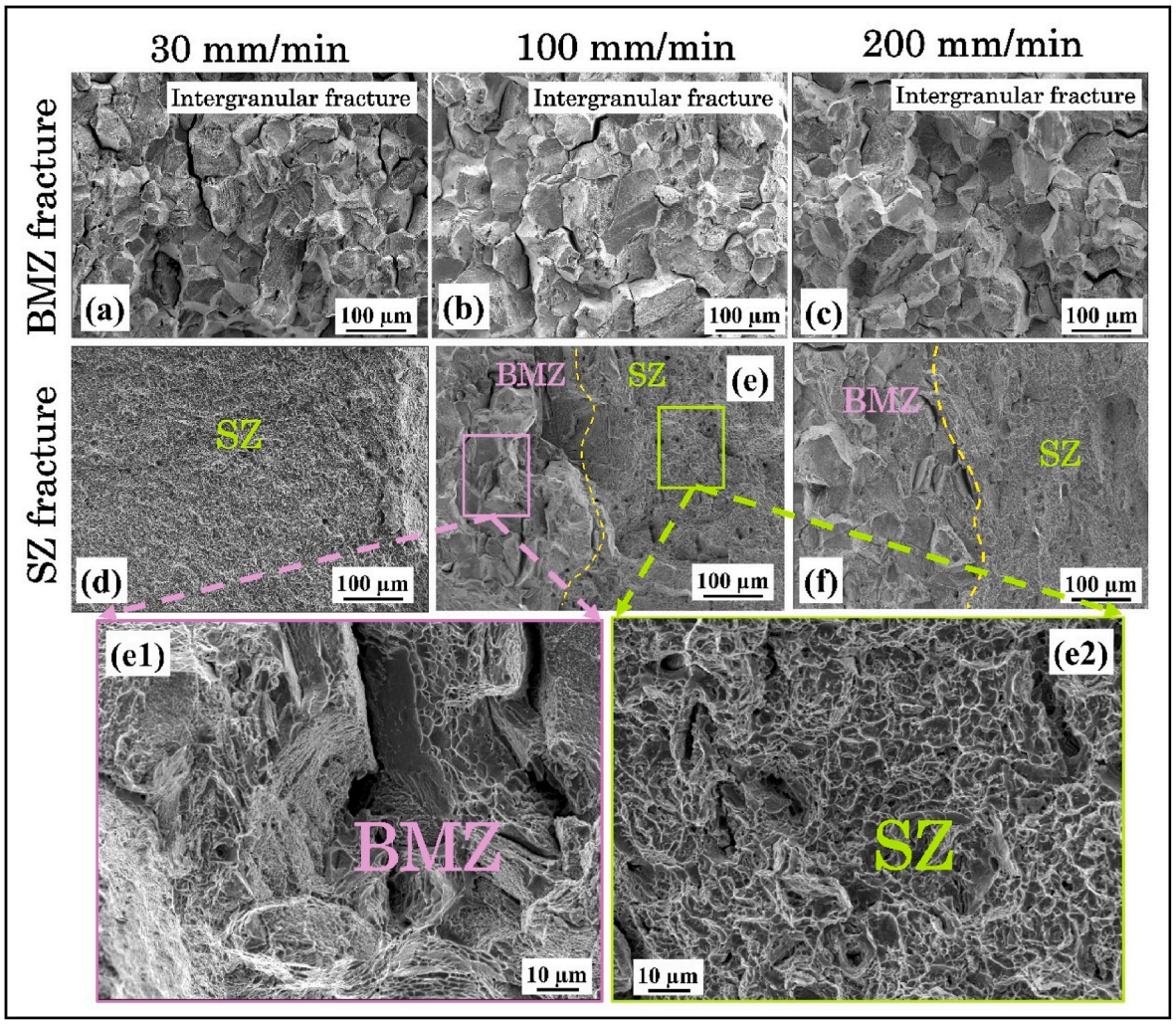

Fig. 11. Low magnification SEM fractographs of PWHT (a–c) BMZ, and (d–f) SZ fractured specimens welded at different welding speeds. e1 and e2 represents the high magnification SEM micrographs from the BMZ and SZ regions of the SZ fractured specimen welded at 100 mm/min, respectively.

ductile intergranular fracture in the base metal region at the bottom of the weld zone. These base metal regions exhibit fracture behaviour similar to that of the BMZ fractured specimens, which is why they are labelled as BMZ in Fig. 11(e) and (f). Fig. 11 (e1 and e2) displays the high magnification micrographs depicting a coarse-grained and fine-grained intergranular ductile fracture in these base metal regions and the stir zone of the SZ fractured specimens welded at 100 mm/min welding speed.

Fig. 12(a–c), (d-f), and (g-i) show the high magnification fractographs of the SZ fractured specimens FSWed at a welding speed of 30, 100 and 200 mm/min, respectively. At all welding speeds, the GB tearing with the fine dimples can be observed, confirming the specimens' ductile intergranular fracture. The other characteristic features involve the fracture of coarse intergranular MC carbides shown in Fig. 12(b), (e), and (h). Fig. 12 (f and g) shows the intergranular void coalescence occurring at multiple locations. The fracture mechanism involving void nucleation, growth, and coalescence at the grain boundaries in the SZ and BMZ fractured specimens is discussed in the next section.

4. Discussion

4.1. Void nucleation, growth, and coalescence

Figs. 13 and 14 show the SEM micrographs of the longitudinal cross-section of the BMZ and SZ fractured specimens, respectively. Void nucleation in the BMZ and SZ fractured specimens occurs either through the decohesion of MC carbides from the matrix or via cracking within the MC carbides themselves [21]. Both mechanisms are driven by stress concentrations resulting from crystallographic features and deformation patterns. Intergranular MC carbides, due to their higher stiffness compared to the matrix, are the primary sites for void nucleation. Noell et al. [22] suggested that the greater the stiffness of the particle relative to the matrix, the higher the stress concentration due to deformation incompatibility. Additionally, coarse intergranular MC carbides are more prone to cavity formation than the finer $M_{23}C_6$ carbides, which are also less stiff [23]. Consequently, during loading, strain localization at the grain boundaries leads to void nucleation, primarily at the MC carbide/matrix interface, as shown in Figs. 13 and 14.

As seen earlier in Fig. 6, the dispersion of intergranular MC carbides in the BM differs significantly from that in FSWed specimens. In the BM specimen, the MC carbides are arranged along the GBs in a colony-like pattern, whereas, in FSWed specimens, they are individually dispersed along the grain boundaries. This pattern is also evident in Figs. 13 (a) and 14 (a). In the BMZ fractured specimen, during loading, voids nucleate at multiple MC carbide/matrix interfaces within an MC carbide colony. The interparticle distance within these colonies is smaller compared to that in the SZ fractured specimens. As a result, intense strain localization occurs in the intervoid ligaments, causing immediate void nucleation followed by coalescence. Joesph et al. [24] also reported

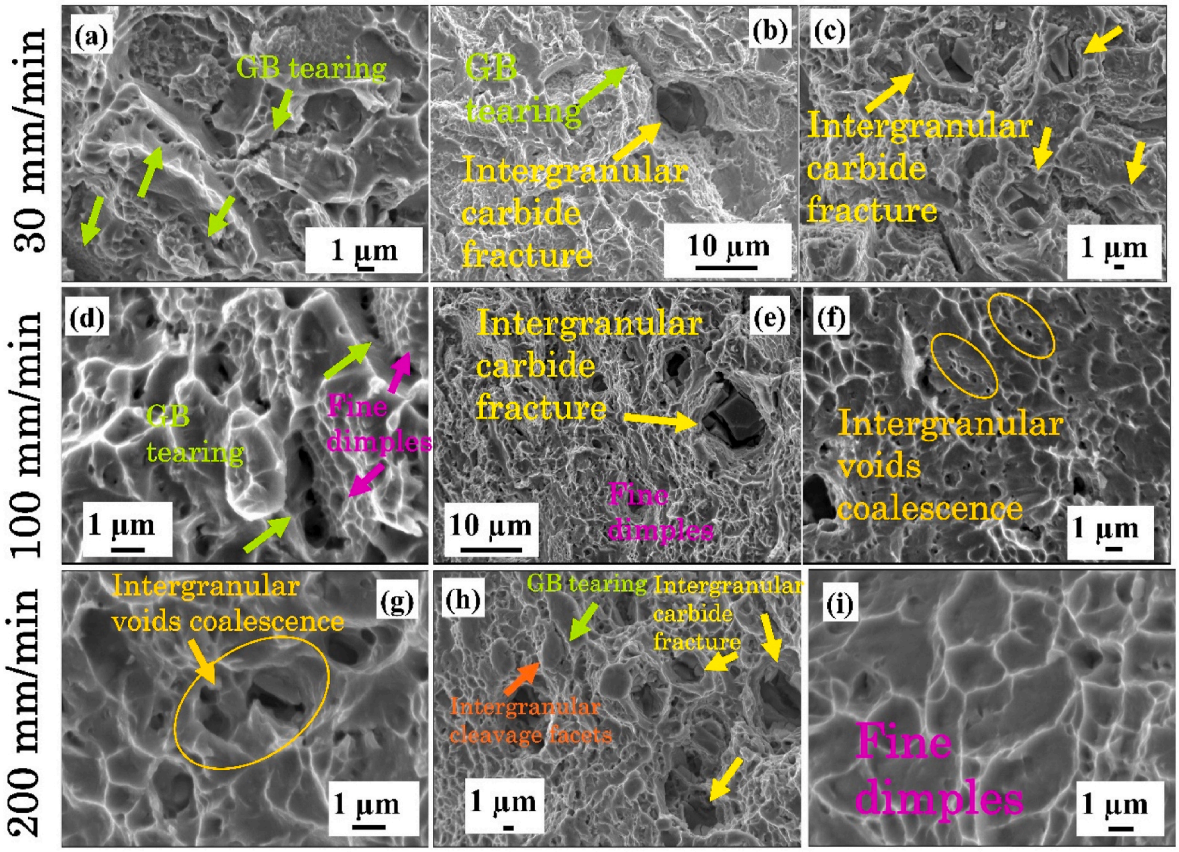

Fig. 12. High magnification fractographs of the PWHT SZ fractured specimen welded at (a–c) 30, (d–f) 100, and (g–i) 200 mm/min, respectively.

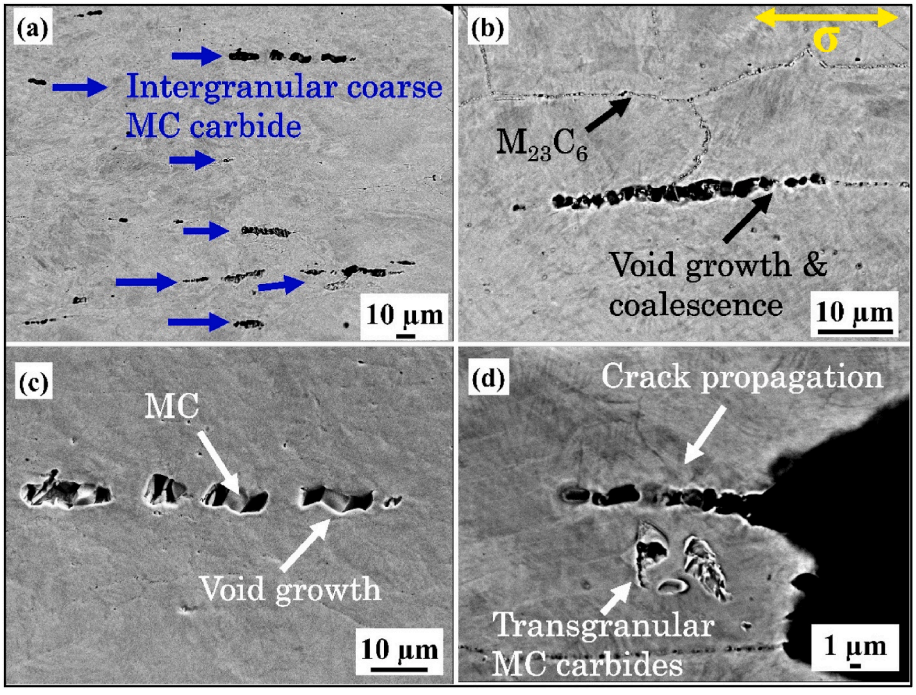

Fig. 13. (a–d) SEM micrographs of the longitudinal cross-section of the PWHT BMZ fractured specimen.

that the interconnected structure of brittle carbides facilitates the easier propagation of cracks originating from the localized fracture of carbides. In contrast, in the SZ specimens, the large intervoid ligaments (due to the distribution of carbides) prevent macroscopic void coalescence. The presence of short intervoid ligaments in the BMZ specimen is evident in Fig. 13 (c), while the coalescence of large intergranular MC carbides is shown in Fig. 13 (b), and crack propagation along the coalesced MC carbides is visualized in Fig. 13(d).

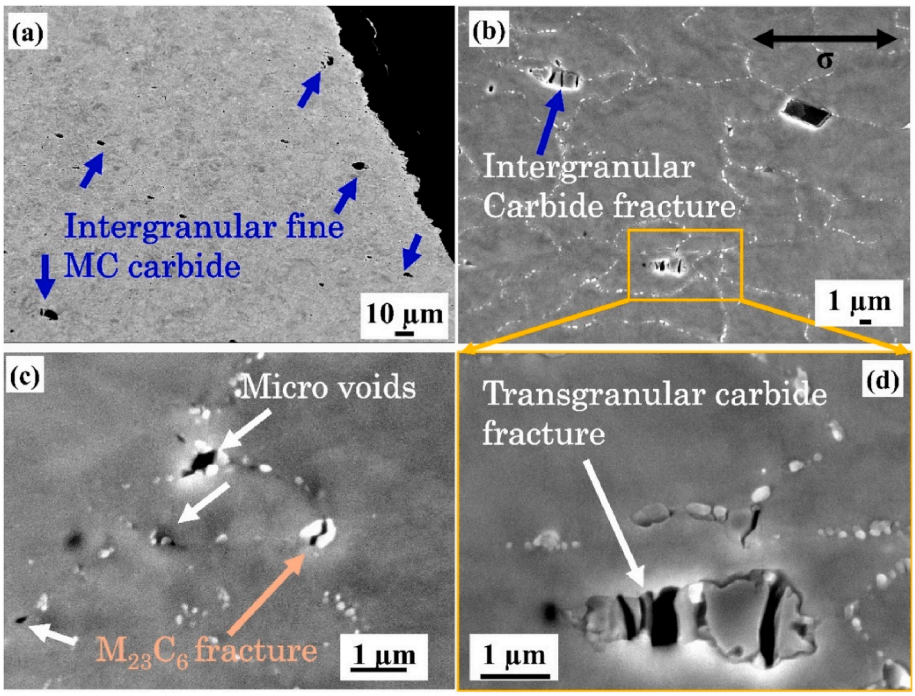

Fig. 14. (a–d) SEM micrographs of the longitudinal cross-section of the PWHT SZ fractured specimen FSWed at 100 mm/min.

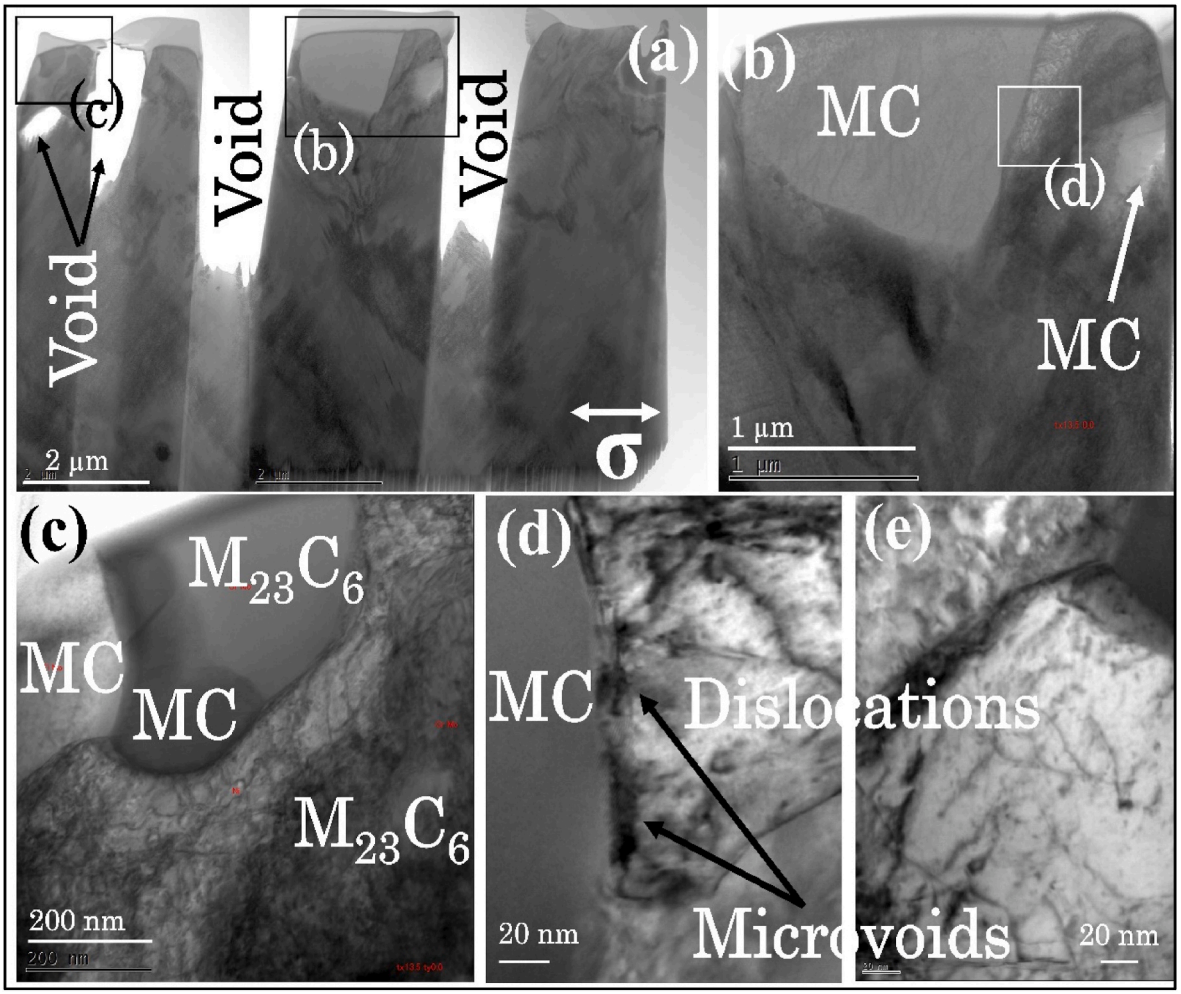

Fig. 15. (a–e) Bright field (BF) TEM micrographs of the base metal region in the SZ fractured specimen welded at 100 mm/min welding speed.

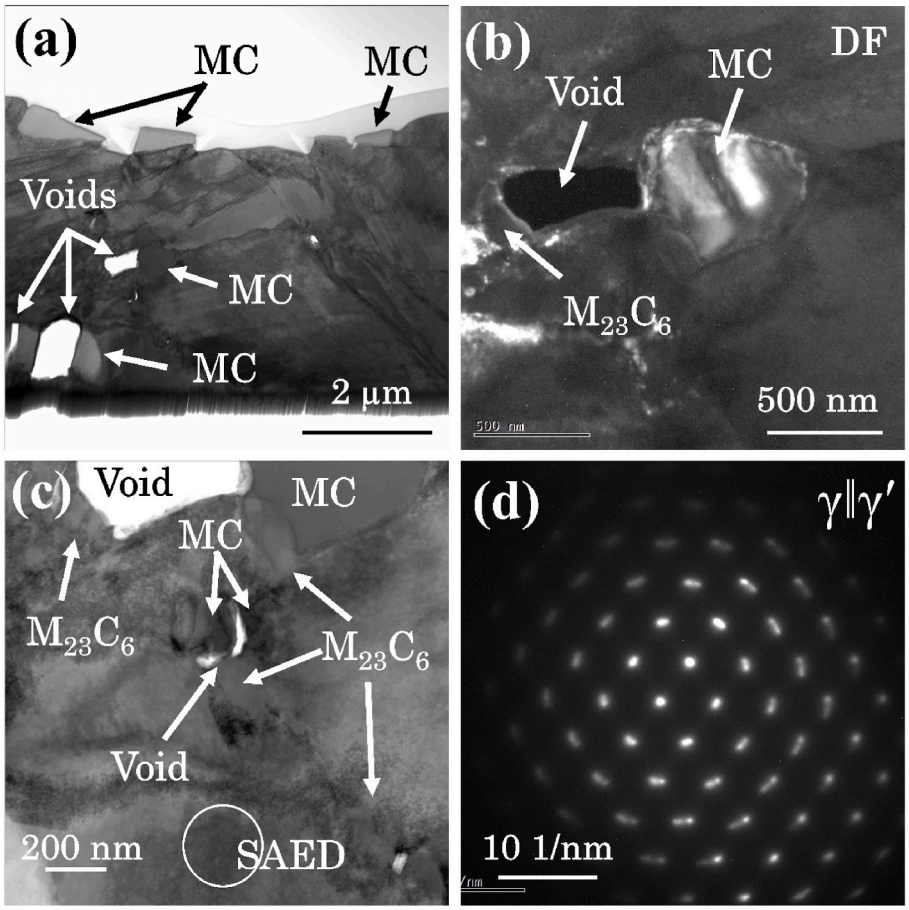

Fig. 16. (a,c) Bright field, (b) dark field TEM micrographs of the SZ region in the SZ fractured specimen welded at 100 mm/min welding speed, (d) represents the SAED pattern from the region indicated in (c).

Fig. 14 (b) represents the restricted growth of the voids owing to the large interparticle separation distance of the MC carbides. In the absence of critical-sized voids, the growth is hindered and thereby the strengthening can be achieved. Fig. 14 (c) demonstrates that not only the MC carbides, but the Cr-rich $M_{23}C_6$ carbides also lead to the intergranular void nucleation by debonding and fracture when the particle size is critically larger. However, the voids nucleated at the $M_{23}C_6$ particle/matrix interface are microvoids and their growth and coalescence are not very detrimental to the strength. Figs. 13 (d) and 14 (d) show that although the particles are dominantly dispersed at the grain boundaries, still some particles are dispersed transgranular and contribute towards the fracture mechanics of the alloy. These observations are further explained in more detail by the TEM characterization of the fractured specimens as follows.

Figs. 15 and 16 display TEM micrographs of specimens obtained from the fractured tensile specimen welded at 100 mm/min. Fig. 15 illustrates the fracture characteristics of the BMZ, while Fig. 16 shows the fracture features associated with the SZ. The TEM specimen for Fig. 15 was extracted from an intergranular carbide colony that includes voids as well as MC and $M_{23}C_6$ carbides. In Fig. 15(a), the large average void size of approximately 1.5 μm at the carbide colonies is evident. Additionally, the carbide colony consists of both MC and $M_{23}C_6$ carbides of varying sizes. Fig. 15(b) and (d) reveal the initiation of microvoids at the interface between the MC carbide and dislocations. These microvoids grow and coalesce with neighboring voids as loading continues, ultimately leading to particle/matrix decohesion.

Fig. 16 presents TEM micrographs from the intergranular MC carbides located in the SZ. The bright regions in Fig. 16(a) indicate voids associated with the corresponding MC carbides. Fig. 16(b) provides a dark field micrograph showing both the MC carbide and the void. The average void size in the SZ is approximately 0.5 μm, suggesting that void growth is more restricted in this region compared to the BMZ fractured specimen. Furthermore, the intervoid ligaments (i.e., the distance between two voids) are larger in the SZ than in the BMZ, as confirmed by Fig. 16(a). Fig. 16(d) shows selected area electron diffraction (SAED) data from the region in Fig. 16(c), revealing the coherency between the γ matrix and γ′ precipitates, as indicated by the characteristic diffraction pattern.

Figs. 15 and 16 provide critical insights into void size, intervoid ligaments, dislocations, and the particle/void interface in both the SZ and BMZ of the FSWed specimen. The intergranular MC carbides are identified as the primary source of void nucleation, which leads to intergranular ductile fracture.

4.2. *Role of grain refinement and secondary carbides*

In the FSWed specimens, the grain size (SZ, ~5–6 μm) is extremely fine as compared to the BM region (~54 μm). Grain refinement during FSW is attributed to dynamic recrystallization driven by plastic deformation and frictional heating [25,26]. The high stored energy generated by plastic flow and frictional heating provides the necessary driving force for dynamic recrystallization, resulting in the formation of fine equiaxed grains in the SZ of the welds. Additionally, the H282 alloy, being a low stacking fault energy (SFE) FCC metal, recrystallizes more readily during hot working compared to materials with high SFE, such as aluminum alloys [27,28]. The fine-grained microstructure strengthens the weld zone through a well-known grain boundary pinning mechanism (or Hall-Petch strengthening) evidenced by the higher

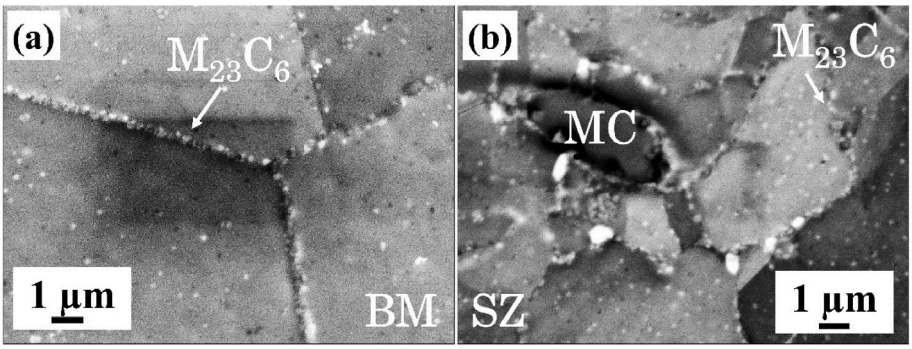

Fig. 17. SEM micrograph comparing the population of intergranular $M_{23}C_6$ carbides in (a) aged BM, and (b) SZ of the specimen FSWed at 30 mm/min followed by PWHT.

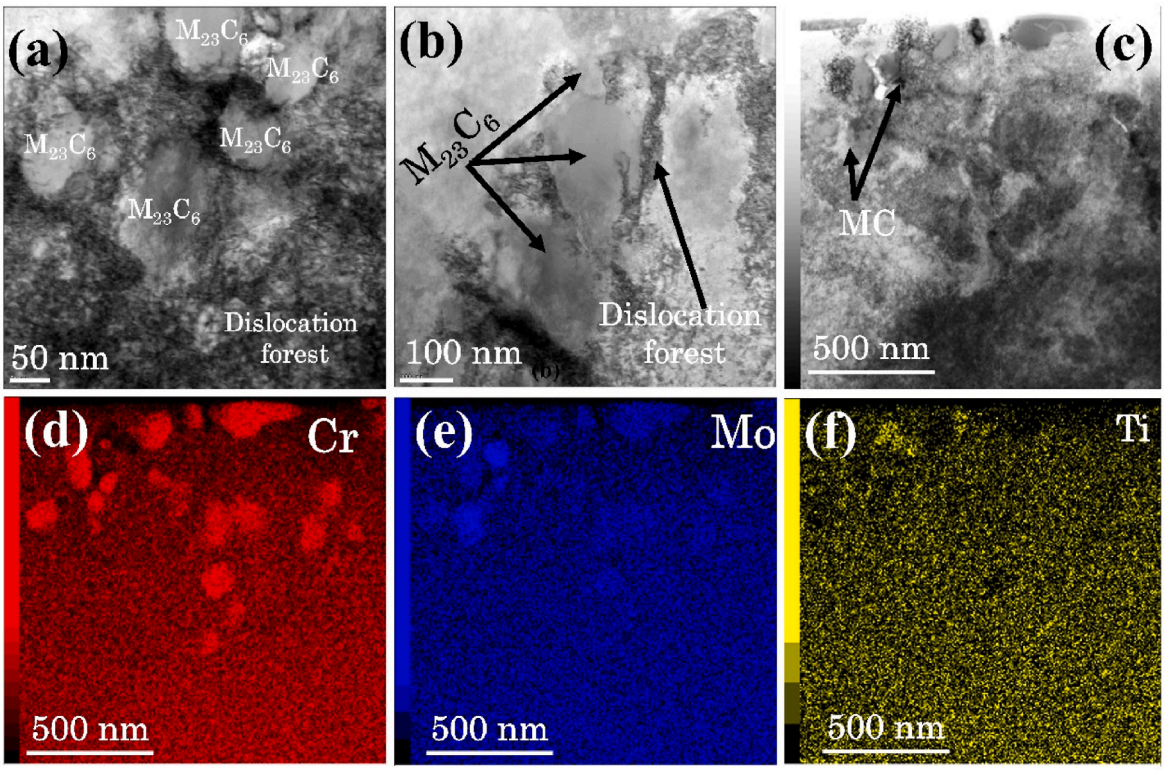

Fig. 18. BF-TEM micrographs indicating a intergranular $M_{23}C_6$ carbides in the SZ of sthe SZ fractured specimen welded at 100 mm/min welding speed, (d–f) EDS elemental mapping of carbides.

microhardness of the SZ (see Fig. 10) and yield strength of the SZ fractured specimens (see Fig. 9 (b)) as compared to the BM.

Another interesting factor related to the fine-grained microstructure is that the grain boundary area is comparatively higher in the FSWed specimen as compared to the BM specimen. During PWHT, the secondary carbides preferentially nucleate at the grain boundaries. Therefore, the fine-grained FSW specimens provide more preferential sites for the nucleation of fine $M_{23}C_6$ carbides at the grain boundaries. The increased precipitation (population) of intergranular $M_{23}C_6$ carbides in the SZ of the FSWed specimen as compared to the BM is evident from the SEM micrographs shown in Fig. 17. These fine intergranular secondary carbides further strengthen the grain boundary by blocking the mobile dislocations and stacking faults that have cut through the fine γ' precipitate [29]. Qin et al. [30] also reported that the population of the carbide significantly affects its strengthening contribution in the total strengthening. Therefore, the strengthening increases with the increase in the population of the $M_{23}C_6$ carbides in the FSWed specimen as compared to the BM specimen. Fig. 18(a–c) indicates the multiple Cr-rich $M_{23}C_6$ carbides occupied at the grain boundary of the SZ. Fig. 18 (d–f) shows the EDS elemental mapping of GB carbides shown in Fig. 18 (c). Interestingly, no void can be observed at the $M_{23}C_6$/matrix interface even though the dislocation density is significantly high as seen in Fig. 18(a) and (b). This observation further confirms that the intergranular $M_{23}C_6$ carbides are less detrimental for the strength of the alloy as compared to the MC carbides during uniaxial tensile loading.

The results and discussions presented above clearly indicate that the welding speed has little impact on the mechanical properties and fracture behavior of the H282 Ni superalloy. This can be attributed to the stable microstructure of the H282 alloy under all the welding conditions used in this study. In other words, the microstructure of the H282 alloy is minimally affected by the amount of frictional heat input typically generated during FSW. This conclusion highlights the merits of FSW over other fusion welding techniques where strict control of process parameters is necessary to prevent elemental segregation in the fusion

zone and HAZ liquation cracking.

5. Conclusions

This investigation documents the friction stir welding (FSW) of Haynes 282 Ni superalloy using a novel hemispherical tool at welding speeds of 30, 100, and 200 mm/min. The key findings are as follows.

(i) The interaction volume and effective plunge depth decrease with increasing welding speed (lower frictional heat input).
(ii) Dynamic recrystallization during FSW leads to significant grain refinement, reducing grain size from ~54 μm in the base metal (BM) to ~10.4, 8.2, and 4.8 μm in the stir zone (SZ) at 30, 100, and 200 mm/min, respectively.
(iii) FSWed joints (PWHT) achieved a tensile strength of ~1360 MPa, exceeding the BM strength of ~1144 MPa, with a UTS based joint efficiency of ~100 %. While welding speed has little effect on strength, joints at 100 and 200 mm/min exhibit higher local elongation than those at 30 mm/min.
(iv) Plastic deformation and material flow during FSW transform intergranular MC carbide colonies in the BM into discrete carbides dispersed at SZ grain boundaries.
(v) Coarse MC carbides act as void nucleation sites, resulting in intergranular ductile fracture in both BM and welded joints.
(vi) The microstructure of H282 alloy is minimally affected by frictional heat input across various process parameters, showcasing FSW's advantage over fusion welding where precise control of process parameters is crucial to prevent elemental segregation in the fusion zone.

CRediT authorship contribution statement

Abhishek Sharma: Writing – original draft, Project administration, Methodology, Investigation, Funding acquisition, Formal analysis, Data curation, Conceptualization. **Yoshiaki Morisada:** Writing – review & editing, Validation, Supervision, Resources, Project administration. **Kohsaku Ushioda:** Writing – review & editing, Supervision, Resources, Investigation. **Sukhdeep Singh:** Writing – review & editing, Resources. **Hidetoshi Fujii:** Writing – review & editing, Visualization, Validation, Supervision, Resources, Project administration, Funding acquisition.

Data availability

All data generated or analysed during this study are included in this published article and its supplementary information files.

Declaration of competing interest

The authors declare that they have no known competing financial interests or personal relationships that could have appeared to influence the work reported in this paper.

Acknowledgment

This work is supported by a Grant-in-Aid for Scientific Research (Kakenhi) from the Japan Society for Promotion of Science (Grant Number 24K17532) and a 2024 Research & Development Grant from the Kyoto Technoscience Center (Grant Number J245403003).

Appendix A. Supplementary data

Supplementary data to this article can be found online at https://doi.org/10.1016/j.msea.2025.148619.

References

[1] S.K. Srivastava, J.L. Caron, L.M. Pike, in: D. Gandy, J. Shingledecker (Eds.), Recent Developments in the Characteristics of Haynes 282 Alloy for Use in A-USC Applications, 2013, pp. 120–130, https://doi.org/10.31399/asm.cp.am-epri-2013p0120.
[2] J. Andersson, G. Sjöberg, M. Chaturvedi, Hot ductility study of HAYNES(®) 282(®) superalloy, in: Superalloy 718 and Derivatives, Wiley, 2010, pp. 538–554, https://doi.org/10.1002/9781118495223.ch41.
[3] J.M. Wilson, C. Piya, Y.C. Shin, F. Zhao, K. Ramani, Remanufacturing of turbine blades by laser direct deposition with its energy and environmental impact analysis, J. Clean. Prod. 80 (2014) 170–178, https://doi.org/10.1016/j.jclepro.2014.05.084.
[4] K.L. Kruger, HAYNES 282 alloy, in: Materials for Ultra-supercritical and Advanced Ultra-supercritical Power Plants, Elsevier, 2017, pp. 511–545, https://doi.org/10.1016/B978-0-08-100552-1.00015-4.
[5] L.O. Osoba, R.G. Ding, O.A. Ojo, Microstructural analysis of Laser weld fusion zone in haynes 282 superalloy, Mater. Char. 65 (2012) 93–99, https://doi.org/10.1016/j.matchar.2011.12.009.
[6] F. Khan, T. Miura, Y. Morisada, K. Ushioda, H. Fujii, Dissimilar joining of A7075 aluminum and SS400 steel utilizing center-driven double-sided linear friction welding using mild steel as a center material: processing, mechanical and microstructure characterization, J. Manuf. Process. 139 (2025) 67–80, https://doi.org/10.1016/j.jmapro.2025.02.017.
[7] C. Joseph, C. Persson, M. Hörnqvist Colliander, Influence of heat treatment on the microstructure and tensile properties of Ni-base superalloy haynes 282, Mater. Sci. Eng. 679 (2017) 520–530, https://doi.org/10.1016/j.msea.2016.10.048.
[8] S. Singh, K. Kadoi, O. Ojo, B. Alexandrov, J. Andersson, The effects of chemistry variations on hot cracking susceptibility of haynes® 282® for aerospace applications, Mater. Des. 228 (2023) 111853, https://doi.org/10.1016/j.matdes.2023.111853.
[9] S. Singh, J. Andersson, Heat-affected-zone liquation cracking in welded cast haynes® 282®, Metals (Basel) 10 (2019) 29, https://doi.org/10.3390/met10010029.
[10] L.O. Osoba, R.G. Ding, O.A. Ojo, Improved resistance to Laser weld heat-affected zone microfissuring in a newly developed superalloy HAYNES 282, Metall. Mater. Trans. 43 (2012) 4281–4295, https://doi.org/10.1007/s11661-012-1212-7.
[11] S. Singh, J. Andersson, K. Kadoi, Microstructure gradient formation in electron-beam melting powder-bed fusion of a gamma-prime Ni-based superalloy, Mater. Char. 205 (2023) 113370, https://doi.org/10.1016/j.matchar.2023.113370.
[12] M. Komarasamy, C. Smith, J. Darsell, W. Choi, S. Jana, G. Grant, Microstructure and mechanical properties of friction stir welded haynes 282, Mater. Char. 182 (2021), https://doi.org/10.1016/j.matchar.2021.111558.
[13] M. Mukuda, A. Noguchi, Y. Morisada, H. Fujii, Development of friction stir welding method using a tilted spherical tool, Sci. Technol. Weld. Join. 29 (2024) 81–88, https://doi.org/10.1177/13621718241231389.
[14] D. Ambrosio, Y. Morisada, K. Ushioda, H. Fujii, Asymmetry in microstructure and mechanical properties of FSWed joints using a hemispherical tool tilted towards the retreating side, J. Manuf. Process. 119 (2024) 32–45, https://doi.org/10.1016/j.jmapro.2024.03.059.
[15] D. Ambrosio, Y. Morisada, K. Ushioda, H. Fujii, Extremely thin intermetallic layer in dissimilar AA6061-T6 and mild steel friction stir lap welding using a hemispherical tool, Sci. Rep. 14 (2024) 1718, https://doi.org/10.1038/s41598-024-52412-w.
[16] A. Sharma, T. Miura, Y. Morisada, K. Ushioda, S. Singh, H. Fujii, Friction stir welding of haynes 282 Ni superalloy by using a novel hemispherical tool, Sci. Rep. 14 (2024) 27826, https://doi.org/10.1038/s41598-024-79331-0.
[17] A. Sharma, Y. Morisada, H. Fujii, Bending induced mechanical exfoliation of graphene interlayers in a through thickness Al-GNP functionally graded composite fabricated via novel single-step FSP approach, Carbon N Y 186 (2022) 475–491, https://doi.org/10.1016/j.carbon.2021.10.018.
[18] D. Ambrosio, A. Sharma, M. Mukuda, Y. Morisada, H. Fujii, Feasibility of friction stir welding using a hemispherical tool tilted towards the retreating side, Journal of Advanced Joining Processes 9 (2024) 100180, https://doi.org/10.1016/j.jajp.2023.100180.
[19] K. Kumar, S.V. Kailas, Positional dependence of material flow in friction stir welding: analysis of joint line remnant and its relevance to dissimilar metal welding, Sci. Technol. Weld. Join. 15 (2010) 305–311, https://doi.org/10.1179/136217109X12568132624280.
[20] H. Takebe, K. Ushioda, Effects of grain size, thickness and tensile direction on ductility of pure titanium sheet, Mater. Trans. 62 (2021) 952–961, https://doi.org/10.2320/matertrans.MT-M2021035.
[21] C. Sénac, Mechanisms and micromechanics of intergranular ductile fracture, Int. J. Solid Struct. 301 (2024) 112951, https://doi.org/10.1016/j.ijsolstr.2024.112951.
[22] P.J. Noell, J.D. Carroll, B.L. Boyce, The mechanisms of ductile rupture, Acta Mater. 161 (2018) 83–98, https://doi.org/10.1016/j.actamat.2018.09.006.
[23] X. Song, Y. Wang, X. Zhao, J. Zhang, Y. Li, Y. Wang, Z. Chen, Analysis of carbide transformation in MC-M23C6 and its effect on mechanical properties of Ni-based superalloy, J. Alloys Compd. 911 (2022) 164959, https://doi.org/10.1016/j.jallcom.2022.164959.
[24] C. Joseph, M. Hörnqvist, R. Brommesson, C. Persson, Influence of carbide distribution on ductility of Haynes®282® forgings, in: Superalloys 2016, Wiley, 2016, pp. 523–529, https://doi.org/10.1002/9781119075646.ch56.
[25] C. Rhodes, Fine-grain evolution in friction-stir processed 7050 aluminum, Scr. Mater. 48 (2003) 1451–1455, https://doi.org/10.1016/S1359-6462(03)00082-4.

[26] A. Sharma, Y. Morisada, T. Nagaoka, H. Fujii, Influence of the number of FSP passes on the strength-ductility synergy of cold-rolled spark plasma sintered pure aluminum, J. Manuf. Process. 79 (2022) 296–304, https://doi.org/10.1016/j.jmapro.2022.04.061.
[27] A. Sharma, T. Das, J. Paul, Performance evaluation of Al6061-graphene nanocomposites surface engineered by a novel multiple microchannel reinforcement approach in friction stir processing, Carbon Lett. 31 (2021) 1111–1124, https://doi.org/10.1007/s42823-021-00230-9.
[28] F. Khan, T. Miura, T. Ito, Y. Morisada, K. Ushioda, H. Fujii, Sound dissimilar linear friction welding of A7075-T6 Al and mild steel by simultaneous interfacial deformation using higher forging speed, J. Manuf. Process. 109 (2024) 512–523, https://doi.org/10.1016/j.jmapro.2023.12.023.
[29] Y. Shimanuki, Precipitation hardening mechanism in Ni-Base wrought superalloys, Transactions of the Japan Institute of Metals 22 (1981) 17–24, https://doi.org/10.2320/matertrans1960.22.17.
[30] X.Z. Qin, J.T. Guo, C. Yuan, J.S. Hou, H.Q. Ye, Precipitation and thermal instability of M23C6 carbide in cast Ni-base superalloy K452, Mater. Lett. 62 (2008) 258–261, https://doi.org/10.1016/j.matlet.2007.05.023.